PHYSICAL REVIEW D VOLUME 23, NUMBER 3 1 FEBRUARY 1981

Electroproduction of $\pi\Delta$ and other nondiffractive final states

C. T. Day,[*] D. J. Harding,[†] J. S. Klinger,[†] L. A..Ahrens,[‡] K. Berkelman, D. G. Cassel, B. G. Gibbard,[‡] D. L. Hartill, J. W. Humphrey,[‡] T. J. Killian,[§] J. T. Linnemann,[‖] E. A. Treadwell,[†] and D. H. White[‡]

Laboratory of Nuclear Studies, Cornell University, Ithaca, New York 14853

(Received 10 September 1980)

This paper reports the results of an experiment measuring the parameters of various electroproduction reactions for a range in the electroproduction variables $0.7 < Q^2 < 4$ GeV^2 and $2 < W^2 < 16$ GeV^2. This report is limited to nondiffractive exclusive channels, with detailed results regarding the $\pi\Delta$ final states, statistically limited results for $K\Lambda$ final states, and upper limits on the production of a number of event topologies containing a single unseen neutral particle.

I. INTRODUCTION

A number of studies have been made of multiparticle final states in deep-inelastic electron scattering.[1] As in almost all particle-physics topics, the interpretations of the results of these studies are limited by the range of the kinematic variables available. This experiment makes use of a large-aperture magnetic spectrometer with limited particle-identification capability to study a wide variety of multiparticle final states in deep-inelastic electron scattering. The results of this experiment extend the range in Q^2 (the four-momentum transfer squared) and W^2 (the invariant mass squared of the hadron final state) of previous studies.

In this paper a simplified overview of the detector, the analysis, and the global features of the data are presented. In addition, results are presented for certain exclusive nondiffractive final states. These results include a detailed study of the production of $\pi\Delta$ final states with comparisons to other data and models, and an approximate determination of production cross sections for $K\Lambda$ and $K\Lambda^*$ final states. Upper-limit estimates of the cross sections for a number of additional exclusive channels are made.

II. APPARATUS DESCRIPTION

The following brief description of the apparatus is intended as general orientation. Those interested in the details are referred to the comprehensive paper on this subject.[2]

In this experiment, an 11.5-GeV/c electron beam was directed onto a 7.5-cm liquid-hydrogen target. The beam-spot size at the target was approximately 1 mm in diameter and its angular divergence was ± 1 mrad. Great care was taken to minimize the beam halo as measured by scintillation counters surrounding the beam pipe immediately upstream of the experiment. The average beam intensity was 5×10^7 electrons per second, with a duty factor of about 5%. The hydrogen target itself was 2 cm in diameter and was positioned near the beam entry point into a large dipole magnet as indicated in Fig. 1. The mag-

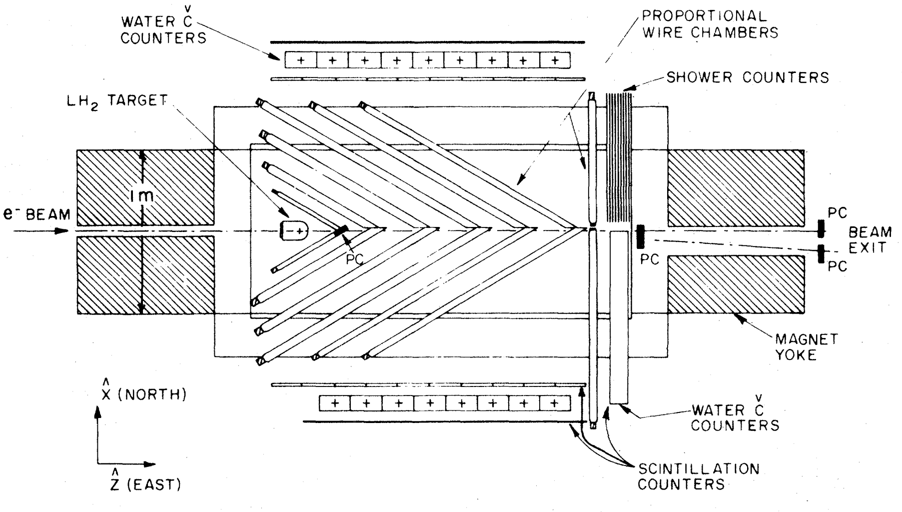

FIG. 1. The apparatus in plan view.

net, with a field volume of 244 cm × 102 cm × 61 cm, was oriented so that the incident beam entered through one yoke and the unscattered beam exited through the yoke at the other end. The central field in the magnet was 8.5 kG and a comprehensive field map was required to do charged-particle event reconstruction with the field nonuniformities of ±20%.

The tracking of charged particles through this volume was done with 34 planes of proportional wire chambers. There were planes of three different orientations, vertical, horizontal, and 30 degrees to the vertical, which allowed the resolution of spatial ambiguities. The wire spacing was 1.5 mm with a total of 22 000 wires. A typical momentum resolution of this system was 0.015 $\Delta p/p^2$. Each proportional wire had its own amplifier and latch. A 20-fold parallel buffer system allowed one to store, with zeros suppressed, the data of an entire event in 1 msec.

The trigger consisted of two shower counters made of alternating layers of scintillator and lead. The position of these shower counters, as indicated in Fig. 1, was such that they could be reached only by electrons having undergone a scatter correspondence to a Q^2 greater than some Q^2_{min}. The pulse height required of the summed output of the shower counters determined the minimum energy of triggering electrons and thus served as an aperture in ν and hence an aperture in W^2.

Along the open sides of the magnet and at the downstream side opposite the shower counters, layers of particle identification counters were positioned. There were two layers of counters measuring the time of flight separated by a layer of water Cerenkov counters. For those charged particles which reached the particle identification layers (approximately 1/3 of the observed tracks), a relatively unambiguous π, K, proton separation could be obtained for momenta up to 0.5 GeV/c, and the π/proton separation remained unambiguous up to about 0.8 GeV/c.

All of the numbers used in this section of the paper to characterize the performance of the system are simple averages while the performance parameters, in fact, depended on the various position and angle parameters.

III. EVENT-RECONSTRUCTION SOFTWARE

A comprehensive description of the event-reconstruction software requires great detail and is dealt with elsewhere.[2] The following brief description of the flow of the lower-level analysis is intended to be helpful in obtaining an overview of the results presented below.

A PDP-11/34 computer was used to read out the hardware and to format the data. In addition, this computer tested each event for the existence of a track which could be an electron. If such a track candidate was found, the event was written on tape, while if no such track candidate was found, the event was discarded.

All further analysis was done in a DEC KI10 computer. The first pass analysis consisted of track-finding. This track-finding was done in the vertical and horizontal planes separately assuming a uniform magnetic field with road widths large enough to compensate for the actual field nonuniformities. Original track paths were determined assuming that the center of the target was a point on the track but the final procedure by which all possible hits associated with a track were found did not make this assumption. The tracks found in the separate planes were then correlated by using the hits in the planes tilted at 30° to the vertical. A final list of the hits which constituted each fully correlated track candidate was then written on tape for later analysis. Events without an identified electron or with no track other than the electron were discarded at this point.

The second pass analysis consisted of a geometric fit to all tracks assuming a common vertex. This global fit used tables which predict the wires hit in each plane as a function of the initial vertex position and the momentum of a track, making use of a full map of the magnetic field. An iterative procedure was followed whereby hits which were not consistent with this overall fit were discarded and the remaining hits refitted. A final event description was obtained which included the vertex coordinates, a list of track parameters, and a full correlated error matrix. These results were then written on tape for further analysis.

For a series of topologies of interest, the next step in the analysis consisted of a kinematic fit. This kinematic fit made use of the energy-momentum conservation constraints and the error matrix to get a best determination of final kinematic variables as well as an estimate of the likelihood that the event belonged in a particular category. These fits were basically of two types: (1) four-constraint fits where all particles are seen, and (2) one-constraint fits where one particle, either charged or neutral, is not seen. Once a particular hypothesis was selected, the degree of consistency of this hypothesis with the available counter information was also determined.

In order to obtain cross sections from the data, it was necessary to determine the total number of incident electrons and to determine the acceptance of the detector. The number of electrons was determined from the total number of counts in a secondary emission quantameter positioned in the unscattered electron beam. This count was recorded on tape and carried along through the analysis. Monte Carlo techniques were used to obtain the acceptance. The effects taken into account in these calculations included the geometric acceptance, the proportional-chamber efficiencies, the efficiencies of the various track-finding and event-reconstruction algorithms, the effects of the event-selection criteria, and the effect of the substantial number of accidental hits in the chambers on all of the above. A more detailed description of these acceptance calculations is given elsewhere.[3]

TABLE I. Sample size at various selection levels.

Incident electrons	5×10^{14}
Raw triggers	8×10^{7}
Events written on tape	3×10^{7}
Electrons reconstructed	3×10^{6}
Geometric fits (two or more tracks)	2×10^{6}
Four-track, net-charge-zero events	1×10^{5}

IV. TOPOLOGICAL EVENT DISTRIBUTIONS

This paper is concerned with the class of events for which there are four tracks with a net charge of zero. Table I indicates how events are lost as one proceeds from the raw triggers down to this sample of interest. For the 1 800 000 events with two or more tracks which satisfied the geometric fit, Table II shows the distribution among the possible observed topologies.

While the ultimate analysis of four-prong net-charge-zero events was via a four-constraint fit, an informative result was obtained in the following way. The 100 000 events of this type were subjected to a three-constraint fit, using the conservation of the three components of momentum. Such fit requires no assumptions regarding the masses of any of the particles and, because of the linearity of the equations, can be done very simply and rapidly. Approximately 15 000 of these events satisfied this fit with a χ^2 of less than 20 for three degrees of freedom.

For these events the shower counter identified the electron but it was necessary to make an assumption as to which one of the two positively charged particles was a proton and then further to assume that the remaining positive and negative particles were both of the same mass. This assumption is correct if all of the particles in the event have been observed and if strangeness and baryon number were conserved. One can then solve for the mass of the unknown pair of particles. In Fig. 2 the result of this calculation is plotted. In those cases where there was ambiguity as to which of the two positive particles was the proton, the selection was made so that the mass of the unknown particles fell nearer one of the known particle masses. In only 15% of the cases it is possible to obtain a distinct real solution for the alternative selection of the particle as proton.

The vertical scale has been changed as a function of mass so that the three distinct peaks which vary in amplitude by more than two orders of magnitude can be simultaneously discerned. The largest peak corresponding to the pion contains 8800 events and is centered about 5 MeV below the mass of the pion. This mass error is probably a result of uncorrected radiative effects which are most important in the calculation of a low mass such as that of the pion. The second largest peak falls at the mass of the kaon to within 1 MeV and contains approximately 1200 events. The smallest peak has 60 events and falls within 1 MeV of the mass of the proton. This peak corresponds to the production of a proton-antiproton pair.[4] The pion and kaon mass peaks have a full width at half maximum of about 30 MeV while the width of the proton peak is somewhat less, perhaps 20 MeV. This plot gives some feeling for how effectively various four-constraint hypotheses are distinguished and some notion of the upper limit on contaminations in them. This plot also gives an indication of the raw number of events of each kind present in our sample before

TABLE II. Percent of events in each topology.

Prongs	Net charge	−5	−4	−3	−2	−1	0	+1	+2	+3	+4
2					10.2		42.9				
3				2.97		16.9		17.9			
4			0.061		1.32		5.44		0.802		
5		0.006		0.080		0.626		0.560		0.061	
6			0.004		0.037		0.109		0.003		0.003
7		0.000		0.002		0.005		0.009		0.002	
8			0.000		0.000		0.001		0.000		0.000

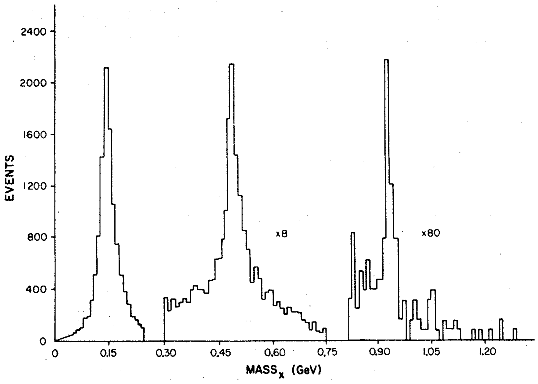

FIG. 2. Mass distribution for x when the reaction is assumed to be $\gamma_v p \to p x^+ x^-$ (note the indicated factors by which the data of higher-mass peaks have been multiplied.)

any fiducial or background suppressing cuts are made. While no acceptance correction has been made the ratio of the peaks 140:20:1 is an indication of the relative cross sections for states which end in π, K, and p, respectively.

V. $\pi\Delta$ PRODUCTION

A. $\pi^-\Delta^{++}$ event selection and corrections

We selected data runs taken under optimum beam conditions, including about half of the total amount of data taken, for a study of the reaction $ep \to e\pi^-\Delta^{++}$. Events with four charged prongs in the final state, two positive and two negative (one being the scattered electron), were tested for energy and momentum balance with the various strangeness-conserving possibilities for the particle identity assignments. A total of 4850 events fitted the four-constraint hypothesis $ep \to e\pi^+\pi^- p$.

Several resonant channels contribute to the $\pi^+\pi^- p$ final state, the most prominent being $\rho^0 p$ and $\pi^-\Delta^{++}$ (see Figs. 3–5). The $\pi^-\Delta^{++}$ state dominates the range of kinematic variables corresponding to $1.35 < M_{p\pi^+}{}^2 < 1.65$ GeV^2, but the yield from other reactions in that range is not negligible. The data for the present study were taken from that range, but with a subtraction of the contribution from other processes which we estimated using a Monte Carlo simulation.

The Monte Carlo calculation also had to account for several other data corrections. The geometrical aperture for triggering on the electron and seeing all four final-state tracks in a sufficient number of proportional chambers depended on angles, momenta, and charges. It averaged about 60% per hadron track. The chamber efficiency was around 90% per track for particles within the geometrical aperture. At the beam intensities chosen for most of the data runs, random uncorrelated background tracks occasionally confused otherwise good event data causing losses in track reconstruction or kinematic fitting. Radiation by the incident or scattered electron caused about 5% of the events to fail the test for momentum conservation. The Monte Carlo calculation also took care of the reduction of electroproduction cross sections to virtual photon cross sections.

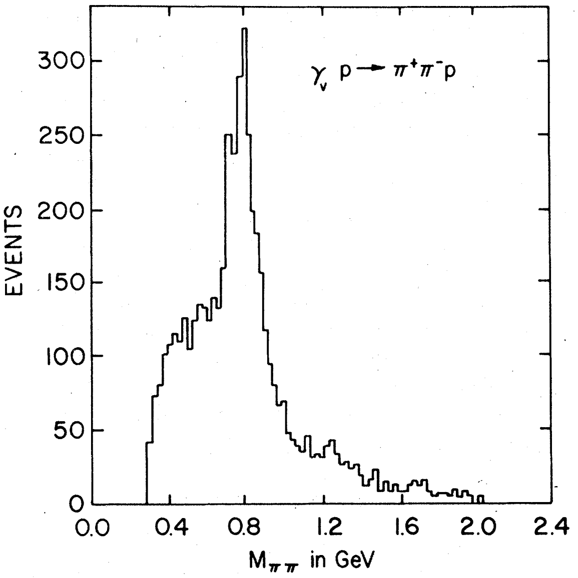

FIG. 3. Distribution in $\pi^+\pi^-$ effective mass for the events used in the $\pi\Delta$ analysis.

The calculation to accomplish all these corrections[5] proceeded as follows. We wrote three event-simulation routines, corresponding to the $\pi^-\Delta^{++}$, $\rho^0 p$, and uncorrelated $\pi^+\pi^- p$ (phase space) hadronic final states. Each was adjusted to mimic

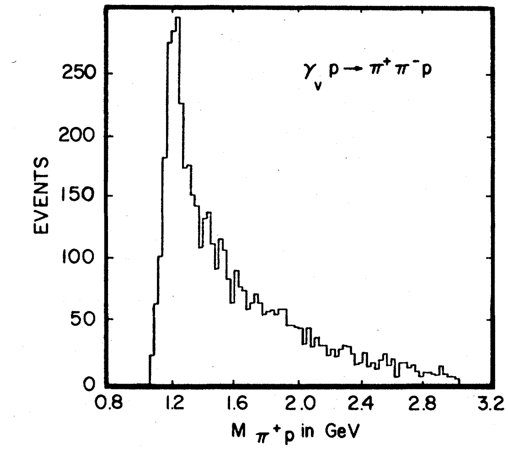

FIG. 4. Distribution in $p\pi^+$ effective mass for the events used in the $\pi\Delta$ analysis.

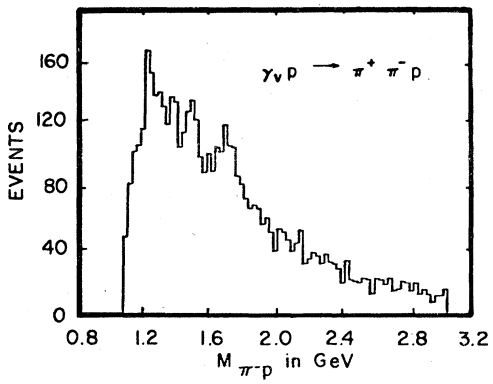

FIG. 5. Distribution in $p\pi^-$ effective mass for the events used in the $\pi\Delta$ analysis.

as closely as possible what is known about the dependence of the yield on the various kinematic variables. In each case events were checked to determine if all final-state particles fell within the required geometrical aperture and if they did the events were accumulated in the same bins of $M_{p\pi^+}$, W^2, Q^2, and angles as were used for the real data. We then performed an overall fit of the binned distributions to the form

$$\text{Real data} = a_1\ (\pi^-\Delta^{++}\ \text{simulation}) + a_2\ (\rho^0 p\ \text{simulation}) + a_3\ (\text{phase-space simulation}),$$

adjusting the three parameters a_1, a_2, and a_3 for the best overall agreement for all of the bins. This then yielded an estimate of the fraction contributed to each bin by the $\pi^-\Delta^{++}$ process. For the bins in the Δ mass peak, $1.35 < M_{p\pi^+}{}^2 < 1.65$ GeV^2, the fraction was typically 60%. In addition, for Monte Carlo-generated $\pi\Delta$ events, the particles produced were propagated through the apparatus, simulating the effects of radiation, scattering, energy loss, nonuniform magnetic field, chamber inefficiency, and the physical boundaries of the detectors. Uncorrelated background hits and tracks were added from a sample of data taken from events which were triggered at random times during the beam spill and final pseudo raw events were recorded. By subjecting these pseudoevents to the full standard analysis, a good measure of the acceptance probability for $\pi\Delta$ events was obtained. The measured cross sections for $\pi\Delta$ production were then obtained from the observed total rate in each such bin, the Monte Carlo-estimated $\pi\Delta$ fractional contribution for that bin, and the acceptance probability for $\pi\Delta$ events generated in that bin.

Since the $\pi\Delta$ measured cross sections derived by this procedure depend on the assumptions made in the Monte Carlo models, we adjusted the $\pi\Delta$ model used in the simulation to agree with the derived cross sections and iterated the procedure. We verified that the effects caused by changes in the model within the range of model uncertainty were generally small compared with the statistical counting errors in the data.

B. $\pi^-\Delta^{++}$ results

In Figs. 6–9 we show the measured cross sections[5] for the virtual-photon reaction $\gamma_v p \rightarrow \pi^-\Delta^{++}$ as a function of W, Q^2, and θ_{π^-} or t, along with data from real photoproduction[2–4] and from electroproduction at lower Q^2.[5] There are no surprises. In each case our new results join on well with the older data where they overlap, or continue previously established trends. The W dependence (Fig. 6) shows a maximum near threshold, shifted perhaps to a slightly higher energy than in the lower-Q^2 data, then a falloff consistent with $(W^2 - M_p{}^2)^{-2}$ at higher energies. Although one might expect s-channel resonances to contribute to the cross section at low energies, there is no evidence for structure in either the W dependence or in the π^- production-angle distributions (Fig. 8).

The decrease in the cross section with increasing Q^2 can be fit to a vector-meson-dominance form

$$\sigma(Q^2) = \sigma(0)/(1 + Q^2/m^2)^2$$

at all but the lowest W. The fits are indicated

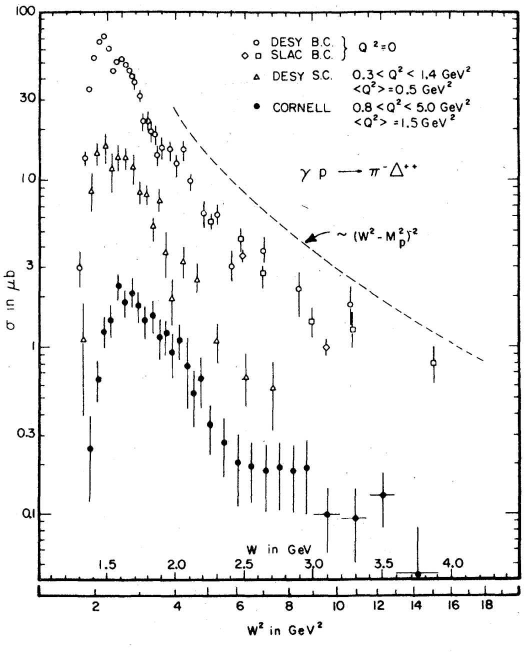

FIG. 6. The cross section for $\gamma_v p \rightarrow \pi^-\Delta^{++}$ as a function of total $\pi\Delta$ center-of-mass energy W. The data of this experiment are compared with data of Refs. 6–8 at $Q^2 = 0$ and Ref. 9 at $\langle Q^2 \rangle = 0.5$ GeV^2.

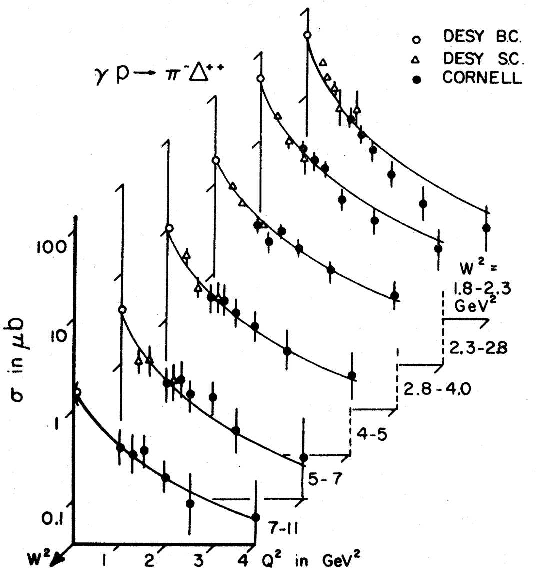

FIG. 7. The cross section for $\gamma_v p \rightarrow \pi^- \Delta^{++}$ as a function of Q^2 for several intervals in W^2. The data of this experiment are compared with those of Refs. 6 and 9. The curves are from the fits of Table III,

by the curves in Fig. 7, and the best-fit mass parameters are given in Table III. In each case m is roughly compatible with the ρ^0 mass ($m_\rho^2 = 0.60$ GeV^2), although tending to increase with W.

At the higher energies the forward peaking of the π^- angular distribution becomes more and more pronounced, so we have plotted it against t, the squared momentum transfer from the virtual photon to the π^- (Fig. 9). The shape is similar to that found in lower Q^2 electroproduction at energies below $W^2 = 7$ GeV^2. There seems to be a mismatch between photoproduction and electroproduction below $W^2 = 7$ GeV^2, perhaps related to the difficulty in comparing data over the same W range.

We examine the decay of the Δ^{++} in terms of polar and azimuthal angles defined in the Gottfried-Jackson frame [9,10] (Figs. 10 and 11). The decay

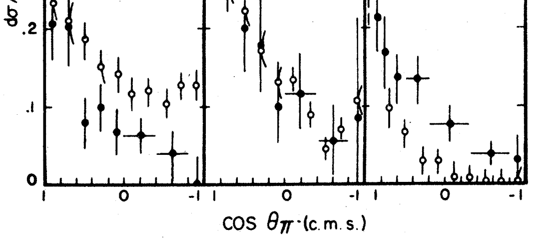

FIG. 8. The cross section for $\gamma_v p \rightarrow \pi^- \Delta^{++}$ differential in the solid angle of the π^- in the $\pi\Delta$ center-of-mass frame, plotted against the cosine of the angle between the π^- and the virtual photon in the $\pi\Delta$ frame. The data of this experiment are compared with the photoproduction data of Ref. 6 (divided by 30).

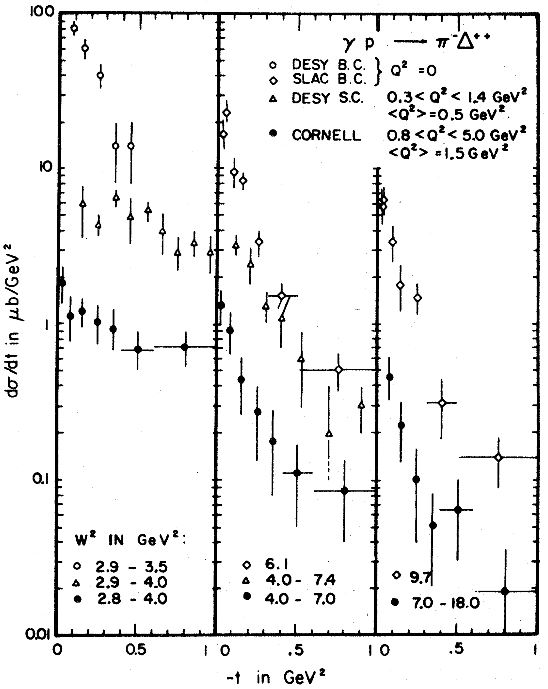

FIG. 9. The differential cross section for $\gamma_v p \rightarrow \pi^- \Delta^{++}$ as a function of t, the invariant four-momentum transfer squared from virtual photon to π^-. Our data are compared with photoproduction data from Refs. 6 and 4 and electroproduction data from Ref. 9. In our case $-t$ actually refers to $-(t-t_{\min})$, where $t_{\min} \simeq -0.6\,Q^2/W^2$. In the other experiments $-t$ starts at zero.

TABLE III. Fits of the Q^2 dependence of $\gamma_v p \rightarrow \pi^-\Delta^{++}$ to the vector-meson-dominance form $\sigma(Q^2) = \sigma(0)/(1 + Q^2/m^2)^2$.

W^2 (GeV^2)	$\sigma(0)$ (μb)	m^2 (GeV^2)
1.8–2.3	45 ± 5	0.46 ± 0.03
2.3–2.8	47 ± 6	0.57 ± 0.03
2.8–4.0	19 ± 2	0.81 ± 0.05
4–5	10 ± 2	0.69 ± 0.08
5–7	4 ± 1	0.66 ± 0.10
7–11	1.5 ± 0.5	1.00 ± 0.23

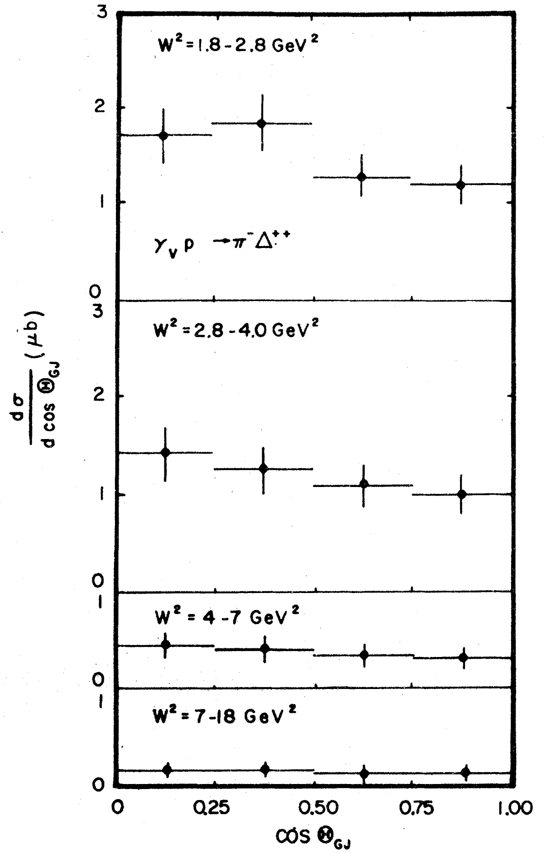

FIG. 10. The measured cross section for $\gamma_v p \rightarrow \pi^- \Delta^{++}$ followed by $\Delta^{++} \rightarrow p \pi^+$, differential in the cosine of the angle between the initial and final protons in the Δ rest frame (Ref. 10), plotted against the cosine.

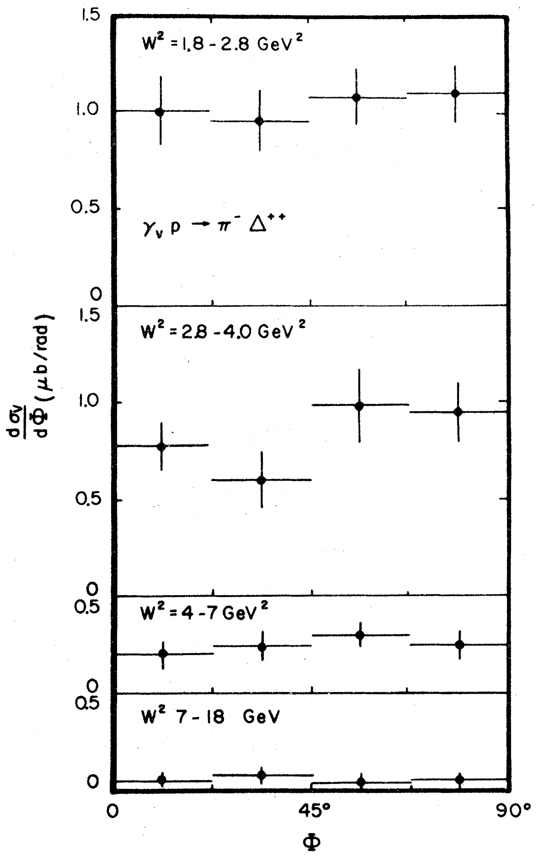

FIG. 11. The measured cross section for $\gamma_v p \rightarrow \pi^- \Delta^{++}$ followed by $\Delta^{++} \rightarrow p \pi^+$, differential in the azimuthal angle ϕ between the plane containing the incident and final proton momenta and the plane containing the virtual photon and the π^- momenta, plotted against ϕ. Since the Δ decay distribution must have the form $a + b \cos\phi + c \cos 2\phi$ (Ref. 10), we sum the data for the four quadrants of ϕ appropriately and plot only for the interval 0 to 90°.

is nearly isotropic at all energies, but shows a weak tendency to favor $\Theta_{GJ} = 90°$ over 0° and 180°. From these distributions we derive the density matrix elements (Figs. 12 and 13) as defined by Wacker *et al.*[9] The results agree with those found in photoproduction[6,11] and in electroproduction at lower Q^2.[5] The dominant matrix element r^{04}_{33} is compatible at threshold with the value 0.375 implied by the Born-contact-term amplitude (one-pion exchange would give $r^{04}_{33} = 0$).[11]

The electric Born model for the process $\gamma p \rightarrow \pi^- \Delta^{++}$, based on the usual three lowest-order diagrams plus the four-particle contact diagram and including absorptive corrections and several s-channel resonances, has been successful in fitting photoproduction data.[11] One expects the virtual hadronic components of the photon to be responsible for the photon absorption, so that when the model is extended off the photon mass shell, the Q^2 dependence should be dominated by the vector-meson-propagator factor $(1 + Q^2/m^2)^{-2}$ with $m \sim m_\rho$. This was found[9] to fit electroproduction data at $\langle Q^2 \rangle \sim 0.5$ GeV^2, and although we have not made a detailed numerical comparison with the model, our distributions in W, t, and Δ decay angles follow the same shapes established at lower Q^2, and our Q^2 dependence is compatible with the vector-meson-dominance prediction. We therefore conclude that the electric Born model continues to be an adequate description of $\pi^- \Delta^{++}$ production up to $Q^2 \sim 4$ GeV^2.

Using PCAC (partial conservation of axial-vector current), attempts have been made[12] to extract the nucleon axial-vector form factor from the $\pi^- \Delta^{++}$ electroproduction data. Since this determination depends mainly on the low-Q^2 behavior of the cross section near the W threshold, our data cannot be used to improve significantly the earlier results.

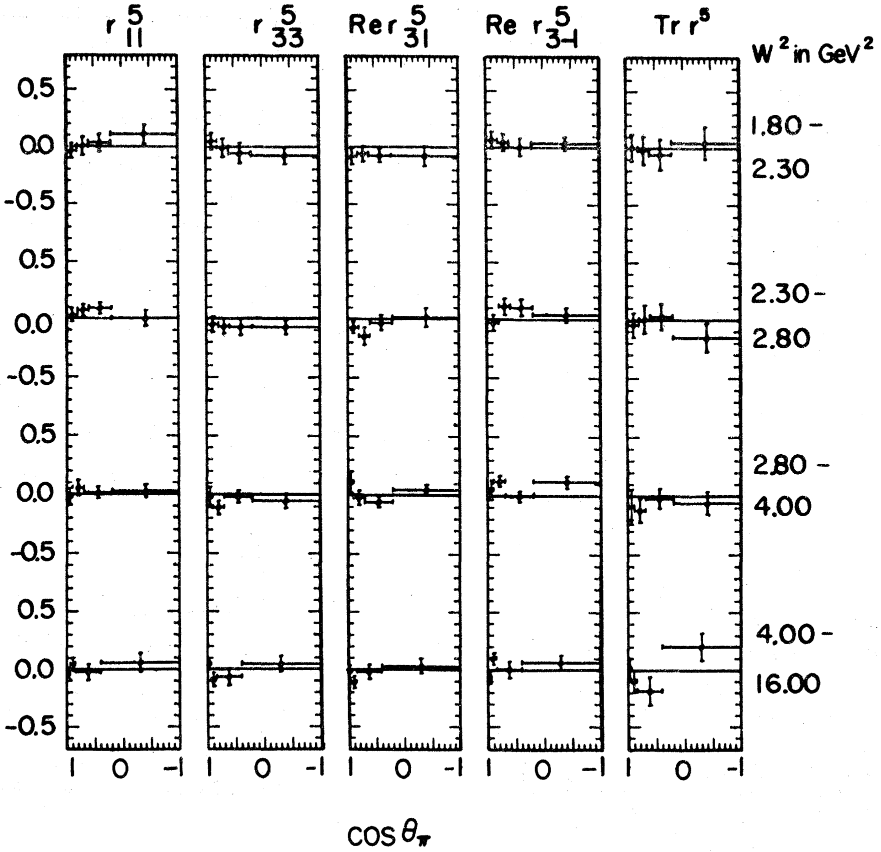

FIG. 12. Density matrix elements in the Gottfried-Jackson system (Ref. 10) for $\gamma_v p \rightarrow \pi^- \Delta^{++}$ followed by $\Delta^{++} \rightarrow p\pi^+$, plotted against the cosine of the angle of the π^- relative to the virtual-photon direction in the $\pi\Delta$ center of mass. The notation is defined in Ref. 9.

C. $\pi^+\Delta^0$ results

The only other $\pi\Delta$ production reaction resulting in an all charged final state is $\gamma_v p \rightarrow \pi^+\Delta^0$, followed by $\Delta^0 \rightarrow p\pi^-$ (one third of the Δ^0 decays). This mode shows up as a small peak at 1.2 GeV in the $\pi^- p$ mass distribution (Fig. 5) along with peaks corresponding to the $\pi^- p$ decay of higher-mass N and Δ states. Since the background under the Δ^0 peak is rather large, we did not try to separate a $\pi^+\Delta^0$ signal and study distributions in W, Q^2, t, etc., as in the case of $\pi^-\Delta^{++}$. We can nevertheless draw conclusions from the observation that the ratio $\pi^+\Delta^0(\rightarrow p\pi^-)/\pi^-\Delta^{++}$ remains small throughout our kinematic range. This ratio would be $\frac{1}{9}$ for production through a $T = \frac{1}{2}$ s-channel resonance decaying into $\pi\Delta$, $\frac{4}{9}$ for production through a $T=\frac{3}{2}$ resonance, and $\frac{1}{9}$ for production via one-pion exchange or the contact diagram. In the naive quark-parton model, if one assumes that the π^+ or π^- is made up of a struck u or d quark from the nucleon together with a d or u member of a pair created from the vacuum, one expects $\frac{8}{3}$ for the measured $\pi^+\Delta^0(\rightarrow p\pi^-)/\pi^-\Delta^{++}$ ratio. Our data, as well as the data at lower Q^2, are consistent only with the one-pion exchange (or contact diagram) and with the $T=\frac{1}{2}$ s-channel resonance mechanisms, and show no evidence for parton behavior. This supports the interpretation of the $\pi^-\Delta^{++}$ data terms of the electric Born model.

VI. $K^-\Lambda^*(1520)$ FINAL STATES

The events found in the kaon peak in Fig. 2 were subjected to a four-constraint fit to the hypothesis $ep \rightarrow epK^+K^-$.[13] When the invariant masses of the various pairs of particles were plotted for those events satisfying this fit, two peaks were observed. As shown in Fig. 14, there is a peak in the K^+K^- mass spectrum which when fit by a Gaussian plus phase-space background has a mass of 1.021 GeV with a σ of 0.011 GeV. This corresponds very well to the ϕ with the width determined by the experimental resolution. In the K^-p mass spectrum, as shown in Fig. 15, there

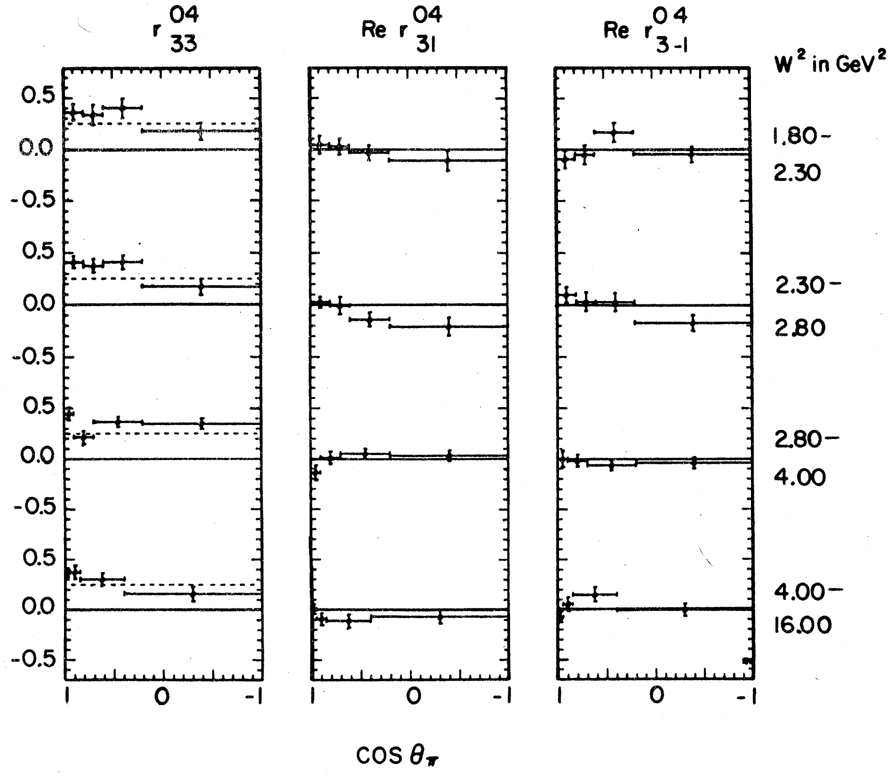

FIG. 13. Density matrix elements in the Gottfried-Jackson system (Ref. 10) for $\gamma_v p \to \pi^- \Delta^{++}$ followed by $\Delta^{++} \to p\pi^+$, plotted against the cosine of the angle of the π^- relative to the virtual-photon direction in the $\pi\Delta$ center of mass. The notation is defined in Ref. 9.

is a peak which has a mass of 1.518 and a σ of 0.011 as determined by a fit to a Gaussian-plus-phase-space background. This corresponds to the Λ*(1520) with the width again determined by experimental resolution.

The ϕ will be considered in another paper and is regarded here as a potential contaminant to the $K^-\Lambda$*(1520) data. This contaminant was removed by requiring that the K^+K^- invariant mass of events used be greater than 1.100 GeV.

The data were divided into two bins in Q^2 for all W^2 and two bins in W^2 for all Q^2. The photoproduction cross section was obtained by weighting each event by the flux factor corresponding to that event. The area of the Gaussian for a fit to Gaussian plus background was regarded as the value of the experimental observation. The acceptance of the system was determined as above by a comprehensive Monte Carlo calculation. Included in the calculation were the various applied cuts. The results are presented in Table IV.

VII. $K^+\Lambda$ FINAL STATES

The reaction $ep \to eK^+\Lambda$ followed by the weak decay $\Lambda \to \pi^-p$ is visible in the detector. The decay vertex is typically separated from the interaction vertex by a distance of more than 10 cm. Such displacements do not significantly affect the acceptance of the hardware. However, the track-finding software developed for this apparatus made use of the known target position as a point of origin for all tracks. While the target constraints were relatively loose and so events of this type were often reconstructed, the acceptance of the total system was drastically reduced for these events.

In Fig. 16 the invariant mass of the π^-p combination for events which satisfied a four-constraint fit to the hypothesis $ep \to e\pi^-pK^+$ is shown. The sharpness and height above background of the Λ peak gives clear evidence that we have extracted such a signal. The acceptance was calculated via a Monte Carlo simulation which took into account the geometry, the detector efficiencies, and the reconstruction and cut requirements. The effect of the improper track-finding algorithm was taken into account by generating events including proper decay vertices and then attempting to reconstruct them with the standard "vertex at the target" track-finding algorithm. While the efficiency depended on W^2 and Q^2 and on the details of the decay distribution, the efficiency

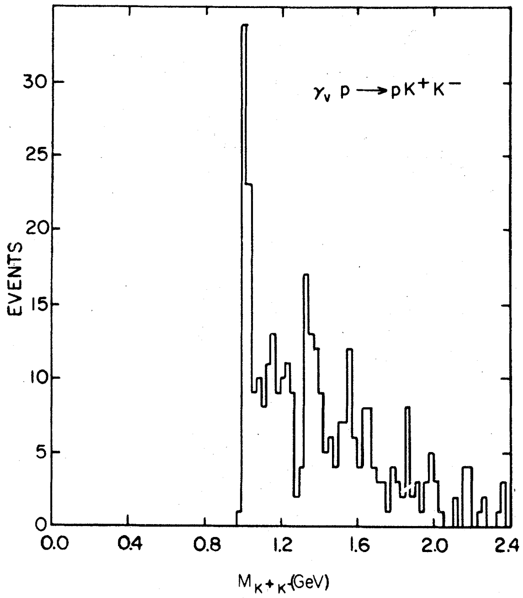

FIG. 14. Distribution in K^+K^- effective mass for events which fit the hypothesis $ep \rightarrow epK^+K^-$.

TABLE IV. $\gamma_v p \rightarrow K^+\Lambda^*(1520)$ total cross section.

$\langle W^2\rangle = 7.03$ GeV^2		$\langle Q^2\rangle = 2.04$ GeV^2	
Q^2 (GeV^2)	σ (nb)	W^2 (GeV^2)	σ (nb)
1.07	63 ± 22	5.25	129 ± 32
2.25	23 ± 7	8.23	30 ± 7

relative to events in which the tracks do all come from the target is 30–40%. An acceptable cross-section measurement was obtained using this standard version of track-finding and reconstruction and the Monte Carlo calculations of the acceptance including these algorithms.

The virtual-photoproduction cross sections for the $K^+\Lambda$ channel were calculated again by weighting each event by the corresponding virtual-photon flux. In Table V these cross sections are given for all Q^2 divided into two W^2 bins and for all W^2 divided into two Q^2 bins. The indicated errors are only the statistical errors. There are in addition uncertainties of the order of 25% in overall normalization and systematic errors associated with acceptance calculations which could be as large as 50%. The most serious problem is the decrease in acceptance by nearly an order of magnitude as one goes from small W^2 to large W^2.

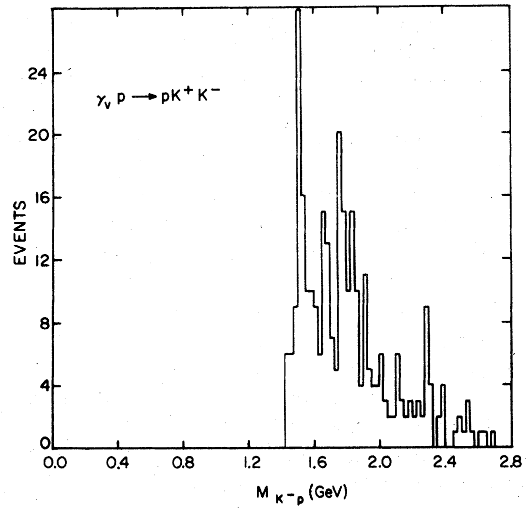

FIG. 15. Distribution in K^-p effective mass for events which fit the hypothesis $ep \rightarrow epK^+K^-$.

VIII. $ep \rightarrow ep\pi^+\pi^-\pi^0$ AND OTHER ONE-CONSTRAINT FINAL STATES

Events containing four charged tracks with a net charge of zero which do not satisfy the energy and momentum conservation equations are candidates for reactions involving a single missing neutral such as $ep \rightarrow ep\pi^+\pi^-\pi^0$ or $ep \rightarrow en\pi^+\pi^+\pi^-$. The fit for these states has only one constraint and thus the sample is very weakly defined. However, in the case where there is a resonance in the final state there is an additional constraint and analysis has been attempted.

The procedure was as follows.[14] Events which

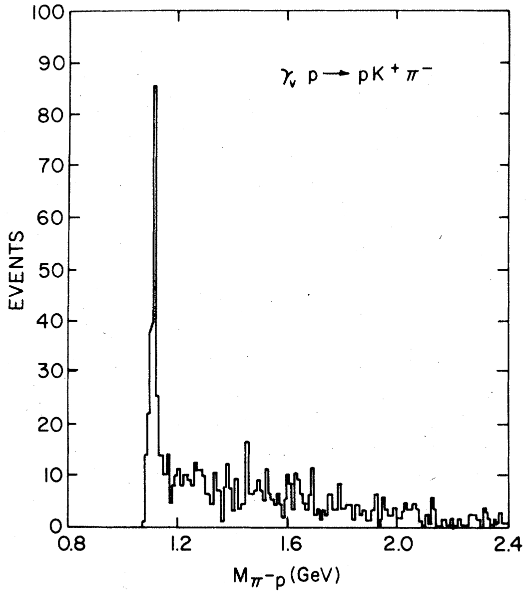

FIG. 16. Distribution in π^-p effective mass for events which fit the hypothesis $ep \rightarrow ep\pi^-K^+$.

TABLE V. $\gamma_v p \rightarrow K^+\Lambda$ total cross section.

$\langle W^2 \rangle = 7.8$ GeV^2		$\langle Q^2 \rangle = 2.4$ GeV^2	
Q^2 (GeV^2)	σ (nb)	W^2 (GeV^2)	σ (nb)
1.0	124 ± 22	3.6	68 ± 10
2.6	51 ± 9	8.0	106 ± 26

TABLE VI. One-constraint cross sections.

Final state	Cross section (μb)
ωp	0.55 ± 0.28
ηp	0.36 ± 0.33
$\rho^-\pi^+p$	0.20 ± 0.30
$\rho^0\pi^0p$	0.28 ± 0.30
$\rho^+\pi^0p$	0.25 ± 0.28

satisfied the one-constraint fit to $ep \rightarrow ep\pi^+\pi^-\pi^0$ were binned according to the invariant mass of various appropriate combinations of final-state particles such as $\pi^+\pi^-\pi^0$ or $\pi^+\pi^-$, etc. This invariant-mass distribution was then fit for a Gaussian resonance shape with a particular mass plus background. The size of the Gaussian contribution was thus a measure of the magnitude of the signal for the particular resonance in the data. In each case where this search for the signal was done a study of the dependence of this signal on the variables Q^2 and W^2 was made. Table VI constitutes a summary of the results of this search.

With the exception of the $p\omega$ final state none of these final states was found to be present with our measurement sensitivity. The details of the $p\omega$ final state are discussed elsewhere.[3] In addition, the signals for other final states were not found to become significant for any of the cuts in Q^2 and/or W^2 that were applied.

A similar procedure was followed looking for Δ final states and looking for resonance-containing final states within the $n\pi^+\pi^+\pi^-$ and $p\pi^+\pi^+\pi^-\pi^-\pi^0$ subsets of the data. In all cases for all Q^2 and W^2 cuts, signals were not observed for cross sections down to the 0.2–0.3 μb level that our sensitivity allowed.

IX. CONCLUSIONS

The results for the electroproduced $\pi\Delta$ final states contain no surprises. The measurements made here are in good agreement with previous measurements in regions of kinematic overlap. The electric Born model continues to give a satisfactory description of the experimental results with this extension in Q^2. The most noteworthy aspect of the results aside from the $\pi\Delta$ is that the nondiffractive electroproduction cross sections are quite small (<1 μb) for each of the exclusive channels studied.

ACKNOWLEDGMENT

This work was supported in part by the National Science Foundation.

---

*Present address: Lawrence Berkeley Laboratory, Berkeley, California 94702.

†Present address: Fermi National Accelerator Laboratory, P.O. Box 500, Batavia, Illinois 60510.

‡Present address: Brookhaven National Laboratory, Upton, New York 11973.

§Present address: EP Division, CERN, 1211 Geneva 23, Switzerland.

||Present address: Rockefeller University Group, CERN, 1211 Geneva 23, Switzerland.

[1] P. Joos *et al.*, Nucl. Phys. B113, 53 (1976); V. Eckart *et al.*, *ibid.* B55, 45 (1973).

[2] L. A. Ahrens *et al.*, Nucl. Instrum. Methods 173, 537 (1980).

[3] J. T. Linnemann *et al.*, Phys. Rev. Lett. 41, 1266 (1978).

[4] B. G. Gibbard *et al.*, Phys. Rev. Lett. 42, 1593 (1979).

[5] A more detailed account of the procedures and results of the $\pi\Delta$ data analysis is given by J. S. Klinger, Ph.D. thesis, Cornell University, 1978 (unpublished).

[6] Aachen, Berlin, Bonn, Hamburg, Heidelberg, München Collaboration, Phys. Rev. 175, 1669 (1968).

[7] Y. Eisenberg *et al.*, Phys. Rev. D 5, 15 (1972).

[8] J. Ballam *et al.*, Phys. Rev. D 5, 545 (1972).

[9] K. Wacker *et al.*, Nucl. Phys. B144, 269 (1978); see also K. Wacker, DESY Internal Report No. F1-76/04, 1976 (unpublished).

[10] K. Gottfried and J. D. Jackson, Nuovo Cimento 33, 309 (1964).

[11] K. Lüke and P. Söding, Springer Tracts Mod. Phys. 59, 39 (1971).

[12] P. Joos *et al.*, Phys. Lett. 62B, 230 (1976).

[13] C. T. Day, Ph.D. thesis, Cornell University, 1978 (unpublished).

[14] D. J. Harding, Ph.D. thesis, Cornell University (unpublished).